Available online at www.sciencedirect.com
SCIENCE DIRECT®
Infrared Physics & Technology 45 (2004) 31–45
INFRARED PHYSICS & TECHNOLOGY
www.elsevier.com/locate/infrared

External cavity tunable diode laser NH_3 spectra in the 1.5 μm region

Li-Hong Xu *, Zhengfeng Liu, I. Yakovlev [1], M.Yu. Tretyakov [1], R.M. Lees

Canadian Institute for Photonic Innovations (CIPI) and Department of Physical Sciences, University of New Brunswick, 100 Tucker Park Road, Saint John, NB, Canada E2L 4L5

Received 29 April 2003

Abstract

NH_3 absorption spectra have been recorded from 6460 to 6522 cm^{-1} at room temperature and ~5.5 Torr pressure with an external cavity tunable diode laser. The spectra served (a) as an initial test of a multipass optical assembly mounted in a large vacuum chamber designed for future slit nozzle experiments, (b) to further our understanding of the characteristics, stability and accuracy of our laser, and (c) to investigate the performance of our system by comparison with previous Fourier transform results. The system sensitivity was high and yielded an average observed line density of over 13 lines per cm^{-1}, about three times greater than reported before, with numerous weak absorptions clearly visible. The lines arise mainly from the perpendicular $(\nu_1 + \nu_3)$ NH-stretching combination band, plus possibly other combinations with excited ν_2 states. Transition wavenumbers, absorption coefficients, and line widths were determined. From extrapolation of trends in wavenumber, intensity and upper state energy for known transitions, 21 additional assignments are proposed for $(\nu_1 + \nu_3)$ band lines. The term values, *l*-doubling and *a–s* inversion splittings for the $(\nu_1 + \nu_3)$ and $2\nu_3$ $(l = 0)$ states in the 1.5 μm region are surveyed. Exploratory fitting was carried out to a linear effective Hamiltonian to assess the extent of off-diagonal interactions and perturbations.

Keywords: Ammonia; Near-infrared; Molecular spectroscopy; External cavity tunable diode laser; Atmospheric trace gas

1. Introduction

In this paper, we discuss near infrared (IR) absorption spectra of ammonia recorded using an external cavity tunable diode laser (ECTDL) operating in the 1.5 μm region. The sample cell consisted of a multipass White cell of 32 in. (0.813 m) base length mounted in a large vacuum chamber, and the present experiments were carried out as a preparatory test of the optical setup using static gas pressure prior to implementing operation of a pulsed slit-jet source for cooled supersonic beam studies.

NH_3 is an important molecule with a rich spectroscopic history. It was the first species to be observed by microwave spectroscopy with the original magnetron of Cleeton and Williams [1],

* Corresponding author. Tel.: +1-506-648-5632; fax: +1-506-648-5948.
E-mail address: xuli@unb.ca (L.-H. Xu).
[1] Visiting scientists from Institute of Applied Physics, Russian Academy of Sciences, Nizhny Novgorod, Russia 603950.

1350-4495/$ - see front matter
doi:10.1016/S1350-4495(03)00176-2

and later was the molecule with which the maser was first developed [2]. Astronomically, it is abundant in the atmospheres of the giant planets [3], was the first polyatomic interstellar species discovered in opening up the field of molecular astronomy [4], and is of great current interest in IR astronomy with the rapid development of high-resolution IR receivers in ground-based and satellite instruments. For example, NH_3 in the Jovian atmosphere has been mapped by the Galileo probe and the Infrared Space Observatory Short Wavelength Spectrometer (ISO-SWS), with interesting differences between the 5 and 10 μm spectral windows as well as an unexpectedly low $^{15}N/^{14}N$ isotopic ratio [5]. In the terrestrial environment, NH_3 is an important atmospheric trace gas. It is a pollutant emitted in certain industrial processes in power stations and fertilizer plants, is relevant to human health control through traces in respiration, and participates in numerous reaction processes in atmospheric chemistry. Therefore, it is of great significance for atmospheric monitoring [6], and is a prominent species in the HITRAN spectral database of major atmospheric molecules [7].

The vibrational fundamentals in the IR absorption spectrum of NH_3 have been intensively studied for many years, and the weaker overtone and combination bands are also receiving a great deal of attention with the development of sensitive Fourier transform infrared (FTIR) and tunable laser techniques. An overview up to the 3 μm region has been presented by Urban [8]. Briefly, in the vibrational notation for D_{3h} molecular symmetry, the v_2 (A_2'') symmetric bending mode at $\sim$950 cm^{-1}, which is the lowest frequency small-amplitude mode, has been investigated extensively [9–12]. A combined analysis blending FTIR and diode laser measurements with microwave, submillimeterwave, diode-laser heterodyne, and infrared–microwave two-photon transition frequencies has provided v_2 wavenumbers for calibration purposes with better than 1×10^{-4} cm^{-1} precision [12]. The v_4 (E') degenerate asymmetric bending mode at $\sim$1626 cm^{-1} has been studied in the microwave region in direct measurements of the *a–s* tunneling splittings between inversion doublet levels [13,14], and in the infrared with grating [9] and FTIR instruments [15]. With the observation of a full band of $\Delta k = \pm2$ forbidden v_4 transitions in the FTIR spectra, the ground-state energies could be accurately determined [15]. These are fundamental to IR studies in which assignments are based on ground-state energy combination differences. High-resolution FTIR NH_3 spectra in the 3 μm region of the v_1 (A_1') symmetric NH-stretch, the v_3 (E') degenerate asymmetric NH-stretch, and the $2v_4$ bending overtone were assigned and partially analyzed in the study by Guelachvili et al. [16]. Empirical power-series modeling was carried out for each of the $2v_4$, v_1, and v_3 states, and a "2, −1" *l*-type parameter was determined from the relative intensities of forbidden $\Delta k = \pm2$ transitions observed for v_3. The 3 μm spectra were recently revisited by Kleiner et al. [17] and reanalyzed by a multi-state approach in which the v_1, v_3, $2v_4$, $(2v_2 + v_4)$, and $4v_2$ states were treated simultaneously.

Above the spectral region of the NH_3 fundamentals, detailed empirical line parameters were reported from 4791 to 5294 cm^{-1} by Brown and Margolis [18]. Some 2000 line positions and intensities at room temperature were measured with precisions of 0.0003 cm^{-1} and 3%, respectively. With additional intensity data from low temperature spectra, empirical energies were derived for the lower and upper states along with their vibrational identities. Somewhat earlier, FTIR results had been reported from 6400 to 6900 cm^{-1} at 0.005 cm^{-1} resolution by Lundsberg-Nielsen et al. [19]. They listed a total of 1700 lines, of which about 380 were assigned based on matches with the ground state energy differences. According to Benedict and Plyler [20], this region should cover the $(v_1 + v_3)$ combination and $2v_3$ overtone bands. Due to the complexity of the spectra, the assigned transitions were reported in increasing frequency order with the *J*, *K* and s/a quantum labels provided for the lower state. The upper vibrational levels were assigned to the $(v_1 + v_3)$ perpendicular band for $\Delta K = \pm1$ transitions and to the $2v_3^0$ $(l = 0 \leftarrow 0)$ parallel band for $\Delta K = 0$ lines. Later, in a cavity-enhanced molecular beam study by Berden et al. [21] with an ECTDL system, low *K* and *J* transition assignments were verified for the $(v_1 + v_3)$ state, and reported for the $(v_1 + 2v_4)$ combination state.

This ongoing strong spectral focus on NH_3 is consistent with a principal aim and application of contemporary molecular spectroscopy, namely to provide comprehensive spectral maps for species of astrophysical and atmospheric importance. Such maps constitute essential data for the sophisticated models of the interstellar medium and planetary and terrestrial atmospheres from which the physical conditions in the host media can be deduced. Reliable modeling of absorption band strengths and profiles requires accurate information on both positions and intensities of spectral lines. However, a difficult problem in calculating accurate band parameters for polyatomic species has always been the presence of a background of weak transitions involving highly excited rotational levels, hot bands and combination bands. These weak lines frequently underlie stronger features used as spectral markers and limit the determination of reliable intensities. Thus, it is important to investigate not only the strong lines providing the major spectral signatures, but also the weaker transitions lying in the ''grass'' in order to get a feeling for their possible effects on the apparent intensities of the strong lines.

Accordingly, in the present study we have re-examined the high-resolution spectrum of NH_3 from 6460 to 6522 cm^{-1}, using an ECTDL source. The measurements also served as the initial test of the multipass optics newly built for our slit nozzle molecular beam system. Most of the strong transitions in this region were reported and assigned in the previous FTIR study [19]. However, our observed average line density of about 13 lines per cm^{-1} includes many new weak features not previously reported, indicating high sensitivity of the combination of the multipass optics with the coherent radiation source. In addition to their intrinsic spectroscopic interest, these weak lines would certainly combine to affect the apparent intensities of the stronger features and thereby reduce the accuracy of line strength determination.

The paper is set out as follows. In Section 2, we describe the experimental details of the use of the ECTDL as a broadband tunable source of IR radiation, and the testing of our multipass optics. In Section 3, various aspects are first discussed of the data reduction scheme developed to enhance the measurement accuracy and frequency linearity through careful calibration of our wavemeter reading against the scanning PZT voltage, and then the observed NH_3 spectral results are presented. In view of the high state density in the region of concern and the numerous perturbations expected, our emphasis at this stage has been on a general exploration of the observed energy patterns rather than a search for new assignments and detailed modeling. The latter will require more extensive background information than is available for this region at the present time. However, we were able to come up with several further plausible $(v_1 + v_3)$ assignments, based on extrapolation of the trends in term values and line intensities. These assignments and the overall excited state $(v_1 + v_3)$ and $2v_3^0$ term value structures with l-doubling and a–s inversion splittings are considered in Section 4, as well as trial results from exploratory fitting of the term values with a simple linear effective Hamiltonian. Lastly, a summary and discussion are presented in the concluding Section 5.

2. Experimental aspects

A block diagram of the experimental setup is shown in Fig. 1. A Newport 2010A external cavity diode laser with DMD1550 laser head (central wavelength of 1.55 μm) was used as the tunable coherent source for a broadband NH_3 spectral scan. A small portion of the laser radiation was split off by a beam splitter (BS) and sent to a Burleigh WA1000-NIR wavemeter (which has a manufacturer-specified precision of ±0.01 cm^{-1} or ±0.001 nm at a centre wavelength of 1000 nm) for readout of wavenumber or wavelength. The main beam was directed to the vacuum chamber in which our multipass optical assembly is installed. The multipass cell follows the design of Hu et al. [22], and has a White configuration with one large and two small spherical concave mirrors each having a 32 in. (0.813 m) radius of curvature. The mirrors have chromium–gold alloy coating on Pyrex and were obtained as a special order from Janos Technology, Inc. The two small end-mirrors are 0.5 in. (12.7 mm) in diameter while the large

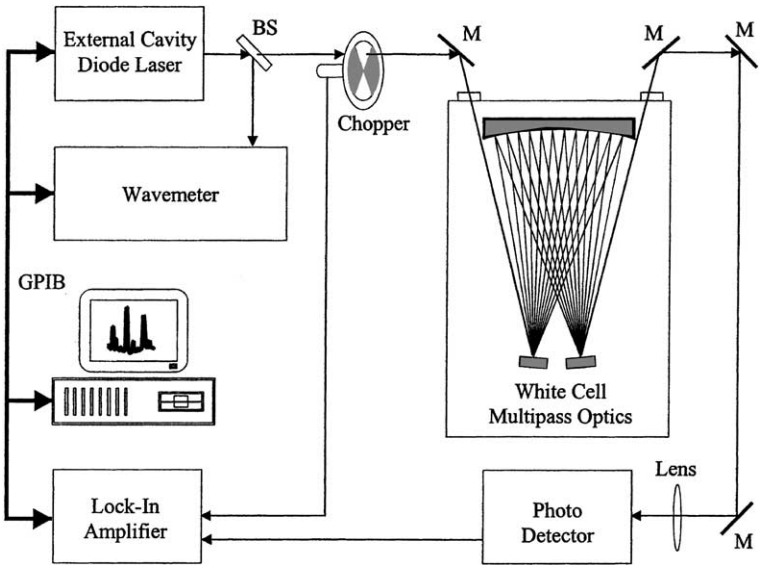

Fig. 1. Schematic block diagram of the experimental setup.

front field mirror is 7 in. (177.8 mm) in diameter with 90% clear aperture. The parameters were chosen so that the entire assembly could be comfortably accommodated within the 40 in. (1.016 m) distance separating the front and back flanges of our six-port vacuum chamber. The chamber is a six-way cross with a spherical body of 27 in. (0.686 m) diameter, with six short arms for flange connections. The estimated maximum achievable number of transits of the multipass cell is 40 for a 2 mm laser beam size. For the present testing of the multipass optics, the vacuum chamber was operated as a static cell, and filled with ~5.5 Torr of anhydrous ammonia from a Matheson lecture bottle. The pressure was chosen to give a balance between the maximum number of absorption lines and a reasonable spectral resolution limited primarily by the Doppler line width. With the optical arrangement for delivery of the ECTDL radiation to the vacuum chamber for the present experiment, we could achieve a maximum of 36 passes which translates to an absorption path length of about 29 m.

The output signal was focused onto a New Focus Nirvana InGaAs photodiode detector operated in single channel mode. After several trials, we decided against the use of laser frequency modulation via the scanning PZT voltage for first or second derivative detection, because the ammonia spectrum in this region is very dense and our trial results showed that the first or second derivative molecular line shapes complicated the observed spectral pattern considerably. Instead, the input laser radiation was mechanically chopped at 2.5 kHz and the voltage signal from the photodetector was demodulated by a lock-in amplifier (Stanford Research Systems, Model SR810 DSP) referenced to the chopper frequency. A computer interface system, using a C program modified from a program originally written in Basic that was kindly supplied by Dr. D. Tokaryk, was set up through a standard GPIB Computer-Board card. The program generates the scan of the laser PZT tuning voltage, reads the laser frequency from the wavemeter, and handles acquisition of the absorption signal data from the digital lock-in amplifier.

In the ECTDL cavity, a diffraction grating is used to diffract the output beam of the laser diode onto a tuning mirror to achieve wavelength selection, and this end cavity mirror is mounted on a piezoelectric tuning element (PZT). Thus, a broadband frequency sweep comprises a succession of smaller scans involving two steps in the

laser tuning: (i) coarse tuning of the angle of the end cavity mirror about a precision pivot by a stepping motor, allowing rotation of the tuning mirror at constant cavity length in order to move the laser to the desired position for the start of a scan, and (ii) fine tuning of the cavity length by varying the voltage applied to the end mirror PZT. Typically, a PZT voltage scan from 5 to 140 V produced about 1.1 cm^{-1} of single mode frequency-tuning in the direction of decreasing wavenumber. Mode hops occurred relatively rarely, and could be in either direction as illustrated in Fig. 2. In a "backward hop", when the PZT scans through a certain voltage the laser frequency hops backwards in a small step to a previous value as depicted in Fig. 2a where the mode hop is marked with †. These were the most common, and simply meant that a small frequency interval was repeated in the mode hop region, seen in Fig. 2b where the second † line is the duplication of the first † line. A "forward hop", on the other hand, leaves a small frequency gap in the spectrum as shown in Fig. 2c. In principle, with careful settings of the laser diode current and temperature, continuous spectral coverage of about 300 cm^{-1} should be achievable for a given laser head according to the manufacturer's specifications. In practice, however, small spectral gaps of approximately 0.05–0.1 cm^{-1} can occur due to forward mode hops, or if the coarse tuning overshoots the desired starting position for the next scan segment. In our experiment, to ensure continuous coverage, we aimed for about 0.1 cm^{-1} overlap between successive spectral scans.

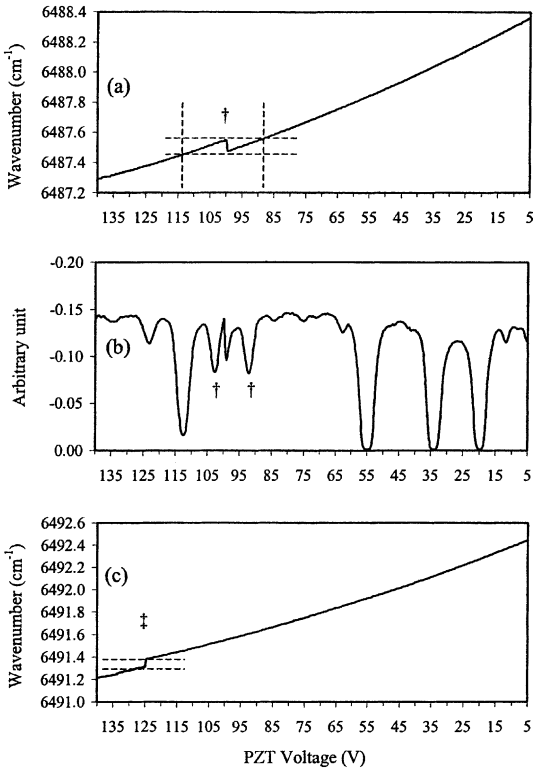

Fig. 2. Appearance of the two types of mode hop: (a) a "backward hop" case. In the plot of laser frequency wavemeter reading against the scan PZT voltage, apart from the apparent laser nonlinearity a small repetition in frequency occurred in the laser mode hop region labeled as †; (b) lock-in signal plotted against the scan PZT voltage where the backward hop produces a duplication of the spectral line labeled as † and (c) a "forward hop" case where a small gap, labeled as ‡, occurs in the plot of wavemeter reading against scan PZT voltage.

In our frequency sweeps, the time interval between consecutive scan points was determined by a combination of hardware and software factors. The principal restriction was the 4 Hz update rate of the Burleigh WA-1000 wavemeter, giving a minimum time of 250 ms for a frequency reading. For our lock-in amplifier, a time constant of 0.3 s gave a good balance between signal-to-noise (S/N) ratio and faithful reproduction of the line shape. A step size of 0.125 V was chosen for the PZT voltage scan from 5 to 140 V, corresponding to 1081 data points in a single spectral segment (approximately 1.1 cm^{-1}). This step size was aimed to give a good compromise between the required scan time and the number of data points needed to adequately define the shape of a spectral line. (Later on in analyzing our spectral data, however, we found in order for the system to respond correctly that a longer interstep delay was required than was actually used. Our readings occurred in pairs with almost equal amplitudes for every two adjacent PZT steps. Thus, in our data reduction scheme, described in the next section, we retained only every second point.) In total, we were able to record a broadband spectral scan from 6460 to 6522 cm^{-1}, representing about 65 overlapping segments, during one working day.

3. Data reduction, frequency linearization, and observations

Our data acquisition program records the scanning PZT voltage, wavemeter reading and lock-in output signal simultaneously. When the wavemeter reading is plotted against the PZT voltage, nonlinearity is prominent, as seen in Fig. 3a. As a result, we see an apparent spectral line width variation in Fig. 3b by almost a factor of two in going from one end to the other of a single 1.1 cm^{-1} spectral scan. This is due to the fact that a 10 V change of laser PZT voltage corresponds to frequency changes of 0.06 cm^{-1} at the high PZT voltage end (125 V) and 0.12 cm^{-1} at the low PZT voltage end (25 V). Although the linewidths look more consistent in Fig. 3c in which the signal is plotted against the wavenumber reading directly, the spectral line profiles do not increase monotonically with the sweep but are distorted with an erratic frequency jitter. This distortion arises because the resolution of the wavemeter is limited to ± 0.01 cm^{-1}, so that fluctuations in the last digit of the wavemeter readout give random back-and-forth jumps in the spectral recording that are an order of magnitude larger than the scanning frequency step size. In practice, such fluctuations in the wavemeter reading might also arise from laser power or spectral variations, mechanical vibrations leading to short-term beam misalignments, etc. However, because the change in wavemeter readout with the PZT voltage has the smooth overall functional form seen in Fig. 3a, we could proceed by fitting the wavenumbers to a polynomial in powers of the PZT voltage. This yielded a well-defined calibration curve that permitted reliable interpolation between the ± 0.01 cm^{-1} limit of the wavenumber readings and in effect acted to enhance the wavemeter resolution. It was found that a polynomial regression gave a good representation of the frequency nonlinearity, and hence gave good interpolated frequencies for each voltage step. When the lock-in output signal was plotted against the linearized frequencies, as shown in Fig. 3d, smooth spectral lines were obtained with consistent line widths. Thus, the full broad-band spectrum could be obtained by performing frequency linearization for each single spectral scan and then piecing the processed spectra together, with amplitude scaling when necessary to compensate for laser power variations in order to give smooth joins from one scan to the next.

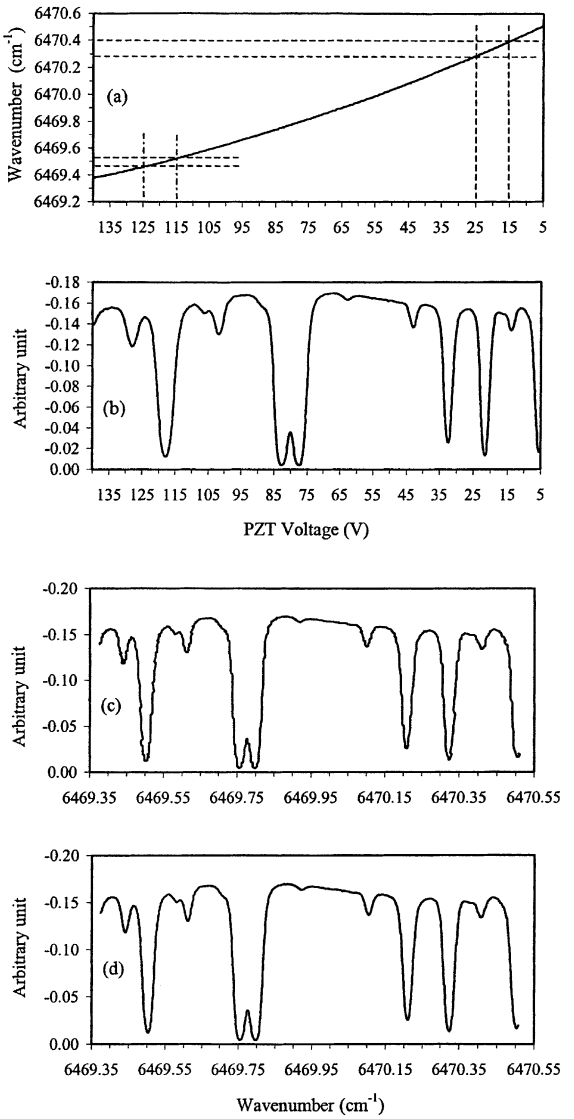

Fig. 3. Illustration of the necessity and procedures for data processing: (a) laser frequency nonlinearity with respect to the scan PZT voltage; (b) lock-in signal against scan PZT voltage, showing apparent non-uniformity in line widths; (c) lock-in signal against wavemeter laser frequency reading, showing noticeable horizontal jitter arising from the limited wavemeter resolution and (d) lock-in signal against linearized laser frequency, showing uniform line widths and removal of frequency jitter.

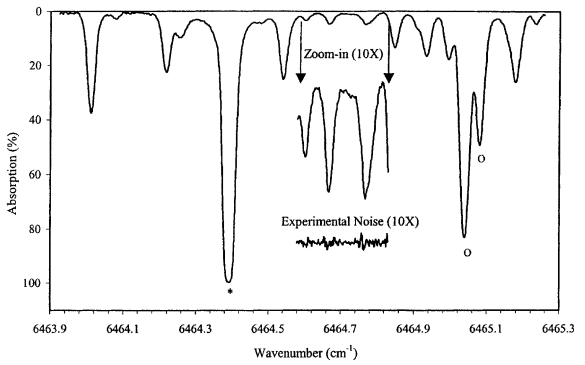

Fig. 4. Sample segment of the observed ammonia spectrum from 6463.9 to 6465.3 cm^{-1}, obtained at 5.5 Torr, room temperature, lock-in amplifier time constant of 0.3 s, and path length of 29 m. The insert shows a fraction (at 10× zoom) of the spectrum with experimental noise. Lines reported in Ref. [19] are marked as (*) – assigned and (o) – nonassigned.

A section of the ammonia spectrum processed as described above is shown in Fig. 4. The inset shows a portion of the spectrum at 10× magnification to demonstrate the sensitivity of the instrument, as well as a 10× trace illustrating the experimental noise. The standard deviation of the noise corresponds to approximately 0.1% of the absorption level. In Fig. 4, the line labeled by (*) at 6464.389 cm^{-1} is the known $(J,K) = (6,1) \leftarrow (7,0)$ s transition to the $l = +1$ component of the $(v_1 + v_3)$ combination state [19]. The lines labeled by (○) were observed but not assigned in Ref. [19]. All other lines, typically of less than 40% absorption, have not been previously reported.

The observed lines in our spectrum were studied in some detail in terms of the centre frequencies, absorption coefficients and line profiles. Each single line was fitted to a Voigt line shape function, with an adjustable term linear in frequency also added to the model to take variations in baseline and the sloping wings of neighbouring lines into account. The effect of line saturation due to the long absorption path was also included according to the Beer–Lambert law. The Doppler width was calculated and used as a fixed parameter in the fit; in our frequency range at room temperature, its value is about 0.019 cm^{-1} (FWHM). Pressure broadening at the experimental pressure of ~5.5 Torr contributes approximately 25% of the observed line widths on average, in accordance with estimates made in Ref. [19]. Broadening due to finite laser line width was considered to be negligible. According to the laser manual, the radiation line width is less than 1 MHz over a 50 ms measurement time and less than 8 MHz for a 1 s interval, very much smaller than the Doppler line width.

Absolute frequency calibration of the spectrum was determined by comparing our data with the previously reported FTIR results [19]. In the earlier study, which employed a Bruker IFS 120 HR Fourier transform spectrometer with 9.5 Torr sample pressure, the absolute accuracy of frequency measurement was about 0.0005 cm^{-1} calibrated against C_2H_2 reference spectra. All of the ammonia transitions observed in Ref. [19] within our spectral range were also observed in our experiment, plus a much larger number of additional weaker lines. For the absolute frequency calibration of our measurements, 159 strong isolated lines observed in both spectra were chosen whose frequencies were not strongly affected by the wings of neighbouring lines. Fig. 5a presents the differences between our measured frequencies and the FTIR results, plotted against the FTIR wavenumbers from Ref. [19]. The differences are seen to have small but systematic positive shifts lying within our wavemeter precision of 0.01 cm^{-1}. The solid line is an empirical polynomial function fitted to the FTIR data, which was used to calibrate our spectra. Fig. 5b then presents the differences between our calibrated wavenumbers and the FTIR data [19]. It is seen that all of the differences lie within ±0.005 cm^{-1}, which we consider to represent the absolute accuracy of our frequency measurements.

From our analysis, we have compiled a listing of the wavenumbers of the line centres, the absorption coefficients and the line widths for the 6460–6522 cm^{-1} region. This list is available from the authors on request. We estimate the accuracy of the molecular absorption coefficients to be in the range of 15–20%. Fig. 6 shows a comparison between a segment of the spectrum calculated with the parameters in our line list table (top trace) and our observed spectrum (middle trace—offset downwards by −20%). The difference between the two (the bottom trace in Fig. 6, offset by −130%) is relatively flat,

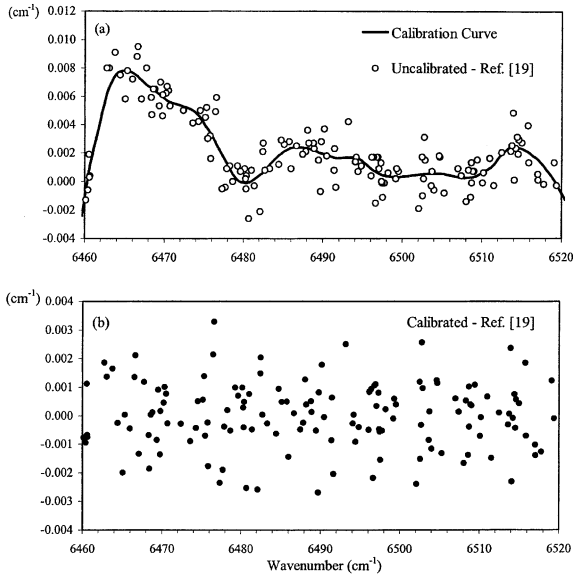

Fig. 5. Frequency calibration: (a) circles represent differences between our measured line frequencies and the FTIR wavenumbers reported in Ref. [19], plotted against the FTIR wavenumbers. The solid line is the frequency calibration function used for absolute frequency calibration of our data and (b) residuals remaining after absolute frequency calibration, representative of our experimental accuracy.

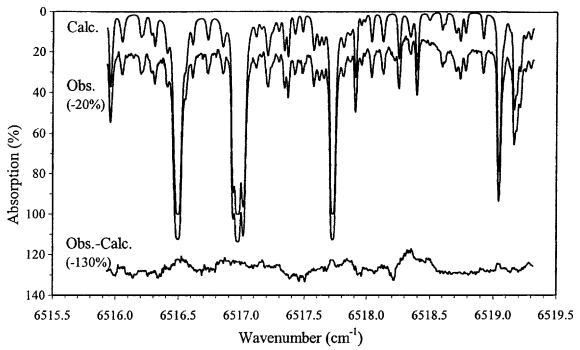

Fig. 6. Comparison between a sample of calculated spectrum (top trace) generated from our line frequency, intensity and width parameters and the experimental spectrum (middle trace—offset downwards by −20% for clarity). The bottom trace (offset by −130%) shows the difference between observed and simulated spectra.

showing that our line parameters give a good representation of the experimental spectrum.

Given that the radiation was introduced to the sample cell via a path of several metres from another room, we expected that there might be some interference due to absorption by atmospheric water. The water lines within our spectral range are well tabulated in the standard HITRAN reference database [7]. However, our spectrum revealed no reduction in apparent intensity in the neighbourhood of the stronger H_2O lines, consistent with the low humidity of a typical dry winter day in New Brunswick. We also did not observe any water signals from absorption within the cell.

4. Energy levels, further assignments, and term value fitting in the 1.55 μm region

The main vibrational bands giving rise to the spectrum in the 1.55 μm region are the $(v_1 + v_3)$ and $2v_3^0$ bands investigated by Lundsberg-Nielsen et al. [19] and the $(v_1 + 2v_4)$ band recently discovered in the jet-cooled study of Berden et al. [21]. These bands are likely to be perturbed by numerous interactions among a variety of overtone and combination states in that region. As described in the introductory section, the fundamental vibrational modes of ammonia are denoted, in D_{3h} molecular symmetry, as v_2 (A_2''), v_4 (E'), v_1 (A_1'), and v_3 (E') in ascending order of energy. Fig. 7a depicts in the first four columns the vibrational energy levels for the four modes individually under the harmonic approximation. The last column collects all of the possible combinations to illustrate the overall density of states. To focus on the region of interest, Fig. 7b gives an expanded view of the energy window (up to second order in overtones) accessed by our present 1.55 μm spectrum.

To explore possible systematic trends in the excited state energy structures in the hope of furthering our understanding of this vibrational region, we compiled energy term value maps for the $(v_1 + v_3)$ and $2v_3^0$ states using the reported wavenumbers [19,21] and ground state energies [15]. The term values for the $(v_1 + v_3)$ combination state are given in Table 1, together with the *l*-doubling for the *s* and *a* components as well as the *a*–*s* inversion splittings for $l = +1$ and $l = -1$ substates. Table 1 also shows *l*-doubling and inversion splittings derived from the results of Guelachvili

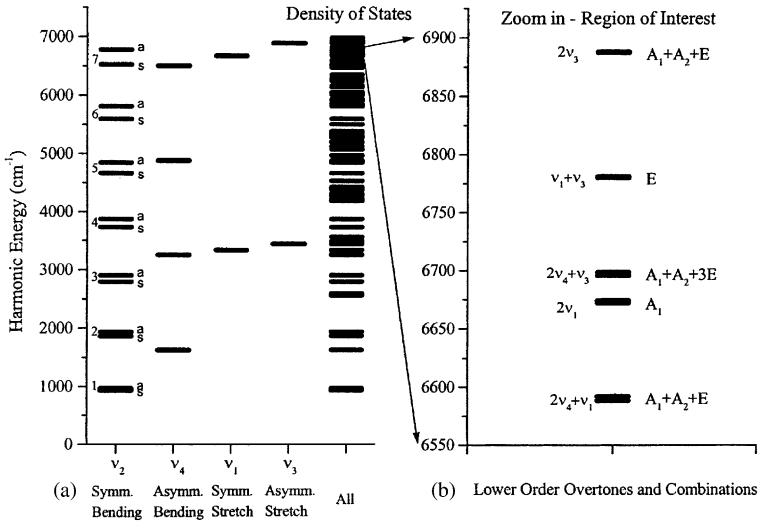

Fig. 7. Density of vibrational states in the region of interest: (a) first four columns show levels for each mode individually; last column collects all possible combinations to illustrate the overall density of states and (b) expanded view of the energy window (up to second order in overtones) accessed by our present spectrum.

et al. [16] for the v_1 and v_3 states individually, for comparison. Table 2 presents the term values for the $2v_3^0$ state, and compares the *a*–*s* splittings to those for the $2v_4^0$ state as determined from published data [16,17].

The $2v_3^0$ term values represent somewhat of a puzzle with respect to the *a*–*s* energy ordering. For a parallel band, the $s \leftrightarrow a$ inversion symmetry selection rule implies that the $s \leftarrow a$ and $a \leftarrow s$ components of an inversion doublet in the spectrum will be separated by the sum of the inversion splittings in lower and upper states, provided the *a*–*s* ordering is the same for both states. For transitions of a perpendicular band, on the other hand, inversion symmetry is conserved, so that a doublet will appear as a significantly closer pair of lines separated just by the difference between upper and lower inversion splittings. For example, the typical line separation is approximately 1.8 cm^{-1} for reported Q-branch doublets in the parallel v_1 band, as compared to about 0.4 cm^{-1} in the perpendicular v_3 band [16]. Now, the $2v_3^0$ spectra belong to a parallel band, as observed by Lundsberg-Nielsen et al. [19], yet for the majority of their assigned doublets the separations are quite small, of the order of 0.2–0.3 cm^{-1}. The $s \leftrightarrow a$ parallel selection rule then results in upper-state energy ordering with the *s* levels higher than the *a* levels, inverted relative to other known states and opposite to the results reported by Coy and Lehmann [23]. In contrast, as shown in Table 2, the inversion splittings that we obtain from the published transition wavenumbers [16,17] for the $2v_4^0$ overtone band do have the expected *a*–*s* ordering.

The $(v_1 + v_3)$ energy patterns in Table 1 display significantly greater irregularities than do those of the individual v_1 and v_3 states. Nevertheless, there is a sufficient measure of systematic behaviour to permit reasonable guesses for several missing levels, notably for $J = K$. We were thereby able to locate candidate transitions to those states from the published FTIR results, and list 21 proposed new assignments in Table 3. Most of these are based on consistency with the wavenumber and intensity trends for associated lines, plus the absence of other plausible candidates in the predicted region. The *a* and *s* labeling for the close ${}^{P}P$ transition doublets with $J = K$ must be regarded as tentative. Four of the upper state levels are accessed by more than one observed IR transition, supporting the assignments via agreement with ground-state combination differences. The $7_1 \leftarrow 8_2$ $l = -1 \leftarrow 0$ *s* transition at 6465.778 cm^{-1} was not reported in Ref. [19] but can be seen in our

Table 1
Term values (in cm^{-1}) for the $(v_1 + v_3)$ state of NH_3, with comparison of l-doubling and a–s inversion splittings for the $(v_1 + v_3)$, v_1 and v_3 states

K	J	$(v_1 + v_3)$ Term values[a,b]				l-Doubling				a–s Inversion splitting				
		$l = +1$		$l = -1$		$(v_1 + v_3)$		v_3[c]		$(v_1 + v_3)$		v_1[c]	v_3[c]	
		s	a	s	a	s	a	s	a	$l = +1$	$l = -1$	$l = 0$	$l = +1$	$l = -1$
0	0			6608.817[d]	6609.747[d]						0.930			0.360
	1			6628.788[d]	6629.657[d]						0.870			0.355
	2			6668.673[d]	6669.432[d]						0.758			0.346
	3			6728.363	6728.993						0.630			0.325
	4			6807.734	6808.279						0.545			0.323
	5			6906.670	6907.378						0.708			0.298
	6			7025.285										0.272
	7			7163.921*										0.245
1	1	6624.612[d]	6625.269[d]	6625.396[d]	6626.308[e]	−0.784	−1.039		−1.151	0.657	0.912	0.990		0.353
	2	6663.552	6665.510[d]	6665.367[d]	6666.165[e]	−1.815	−0.655	−1.165		1.958	0.798	0.987		0.344
	3		6724.411	6725.211	6725.950		−1.539		−1.178		0.739	0.980		0.338
	4	6801.368*		6804.906	6805.842*	−3.538		−1.201			0.936	0.984		0.300
	5		6899.581*	6904.499*	6900.594*		−1.013		−1.171		−3.905	1.009		0.289
	6	7018.781*		7024.268*[e]	7019.672*	−5.487		−1.242			−4.596	1.082		0.266
	7		7155.801	7163.173*[e]	7157.878		−2.078		−1.258		−5.294	1.290		0.239
	8	7310.936*			7314.546*			−1.350				1.817		0.210
2	2	6652.282[d]	6653.147[d]	6654.161[e]	6655.059[e]	−1.878	−1.912	−2.323	−2.305	0.865	0.899	0.992	0.366	0.347
	3	6711.919	6712.576	6713.937	6714.880	−2.018	−2.304	−2.344	−2.321	0.657	0.943	0.984	0.349	0.325
	4	6791.325*	6791.534	6793.700	6793.989	−2.375	−2.456	−2.358	−2.366	0.209	0.289	0.984	0.328	0.336
	5	6889.209	6889.693	6891.968*	6894.197*[e]	−2.760	−4.504	−2.414	−2.432	0.484	2.228	1.003	0.243	0.261
	6	7006.913*	7007.388	7011.805	7010.063	−4.892	−2.764	−2.406	−2.471	0.475	−1.743	1.069	0.318	0.383
	7	7142.411*	7144.876		7146.326		−1.451	−2.654	−2.397	2.464		1.251	0.284	0.027
3	3	6692.402	6693.261	6695.037[e]	6696.154*[e]	−2.635	−2.893	−3.485	−3.457	0.859	1.117	0.996	0.365	0.337
	4	6771.808	6772.429	6775.240	6777.082*	−3.432	−4.653	−3.527	−3.497	0.621	1.842	0.988	0.348	0.318
	5	6870.434	6870.873	6875.312*	6875.294	−4.878	−4.421	−3.582	−3.558	0.439	−0.018	0.998	0.319	0.295
	6	6988.900	6988.953*[e]	6993.076	6993.021	−4.176	−4.069	−3.656	−3.726	0.052	−0.055	1.045	0.196	0.265
	7		7123.521*	7130.519*	7130.458		−6.937	−3.773	−3.693			1.201	0.313	0.234
	8		7280.091	7287.179*				−3.921	−3.856			1.676	0.264	0.200
4	4	6744.764	6745.611	6747.689[e]	6748.706[e]	−2.925	−3.096	−4.653	−4.607	0.847	1.017	1.002	0.371	0.325
	5	6843.861*	6844.392*	6848.313	6848.330	−4.452	−3.937	−4.725	−4.677	0.532	0.017	0.997	0.349	0.302
	6	6960.321*	6961.156*	6968.275	6967.696	−7.954	−6.540	−4.822	−4.776	0.834	−0.580	1.024	0.314	0.269
	7	7098.318*	7098.071*	7107.738	7106.829	−9.420	−8.759	−4.956	−5.017	−0.247	−0.908	1.151	0.170	0.231
	8			7266.749				−5.137	−5.016			1.576	0.322	0.201
5	5	6809.408	6810.247	6812.468*[e]	6813.304*[e]	−3.060	−3.057	−5.816	−5.754	0.839	0.836	1.013	0.371	0.309
	6	6928.216	6928.671	6936.524*	6936.874*	−8.307	−8.204	−6.004	−5.865	0.454	0.351	1.015	0.421	0.282

	7	7066.789	7066.608	7074.922		−8.134	−6.114	−6.037	−0.181		1.093	0.333	0.256
	8	7227.427*	7233.726	7233.330		−6.299	−6.297	−6.382		−0.396	1.732	0.161	0.245
	9			7412.535			−6.613	−7.009			2.425	−0.138	0.257
6	6	6886.302	6887.135				−6.984	−6.900	0.834		1.040	0.376	0.293
	7	7024.808		7035.748	7036.356	−10.940	−7.129	−7.058		0.608	0.882	0.322	0.251
	8	7182.698	7182.302	7193.992		−11.294	−7.355	−7.345	−0.395		1.208	0.245	0.235
	9	7361.533*	7357.645				−7.647	−8.073	−3.888		2.280	0.033	0.458
7	7	6975.409	6976.246				−8.155	−8.033	0.837		1.052	0.381	0.248
	8	7133.638	7133.860				−8.395	−8.288	0.222		1.348	0.327	0.221
	9	7311.763	7310.333				−8.801	−8.740	−1.431		2.164	0.258	0.196
8	8	7076.728	7077.575				−9.361	−9.194	0.848		0.994	0.388	0.221
	9	7254.720	7254.559				−9.909	−9.707	−0.161		1.964	0.326	0.124

[a] Term values were obtained by adding ground state energies from Ref. [15] to reported wavenumbers from Ref. [19] unless otherwise indicated.

[b] Asterisks indicate term values not included in subsequent fitting. These term values are believed to be perturbed on the basis of irregularities in difference table trends or anomalously large (obs–calc) residuals in the fit.

[c] Calculated from term value maps derived from wavenumbers reported in Refs. [16] and [17].

[d] Term value reported in Ref. [21].

[e] New term value proposed in the present work, as given below in Table 3.

spectrum in Fig. 8 as a clear shoulder to the strong saturated feature just above, which is still unidentified.

The term value pattern for the v_3 state in Table 1 is very regular. The magnitude of the l-doubling $|E(l = +1) - E(l = -1)|$ for the $J = K$ v_3 levels is given fairly closely by $1.16K$ and $1.15K$ cm^{-1} for the s and a levels, respectively, with a slow and smooth increase in going to higher J levels. This is in sharp contrast to the rapid and erratic variation with J seen for the $(v_1 + v_3)$ state. However, the magnitudes of the $(v_1 + v_3)$ and v_3 l-doubling are roughly comparable at low values of K, suggesting that for both states excitation of the degenerate v_3 bend is making a similar contribution to the $C\zeta$ parameter.

The a–s inversion splittings vary smoothly but with a relatively strong J-dependence for both the v_1 and v_3 states in Table 1, increasing with J for v_1 and decreasing for v_3. The magnitudes of the splittings for $J = K$ levels are approximately 0.99 cm^{-1} for v_1 and 0.36 cm^{-1} for v_3 as compared to about 0.9 cm^{-1} for $(v_1 + v_3)$ in Table 1, implying that the v_1 mode is the dominant contributor to the inversion splittings for the $(v_1 + v_3)$ combination state. For the $2v_3^0$ overtone state, the inversion splittings in Table 2 are inverted and extremely erratic compared to the $2v_4^0$ values. The lack of any clear pattern suggests the presence of substantial and complex perturbations to the $2v_3^0$ levels.

Although the irregularities in the term value maps indicated significant interactions affecting the $(v_1 + v_3)$ and $2v_3^0$ energy manifolds, we decided in the spirit of Ref. [21] to explore trial modeling of the term values using just the linear diagonal terms in the usual semi-empirical power-series effective Hamiltonian, to see how well the energies could be fitted and to give a sense of the likely extent of perturbations. The levels of s and a inversion symmetry were treated separately, and we excluded data that either had anomalously large residuals or appeared to deviate significantly from trends seen in difference table expansions of the term values. At this basic trial level, we used simply the Solver function in Excel spreadsheets to fit to the term values, rather than a rigorous least-squares analysis. The resulting parameters are listed in Table 4, along with the overall rms standard

Table 2
Term values (in cm^{-1}) for the $2v_3^0$ state of NH_3 and comparison of *a*–*s* inversion splittings for the $2v_3^0$ and $2v_4^0$ states

K	*J*	$2v_3$ $l = 0$ Term values[a,b]		*a*–*s* Splittings[c]	
		s	*a*	$2v_3^0$	$2v_4^0$
0	1	6814.836			
	2		6852.998		
	3	6911.219			
	4		6987.376		
	5	7083.611			
1	1	6811.132	6810.548	−0.584	1.836
	2	6850.605	6849.642	−0.963	2.474
	3		6907.267		2.885
	4	6984.491	6984.039	−0.452	2.583
	5	7080.282	7080.645	0.364	3.015
2	2	6840.868	6839.555	−1.312	2.103
	3	6896.915*			2.945
	4	6974.504	6972.560*	−1.945	4.058
	5	7070.301	7069.913	−0.387	5.161
3	3	6880.935			2.604
	4	6957.880	6957.258	−0.622	3.895
	5	7053.638	7053.231	−0.407	5.289
	6	7168.615*	7168.289	−0.326	
4	5	7032.957*	7030.445	−2.512	3.574
	6	7149.173	7148.870*	−0.303	5.456
	7	7286.445*			7.281
	8	7443.163			
5	5		6999.511		7.232
	6	7116.537	7115.511	−1.026	7.936
	7	7253.476	7251.425*	−2.052	
	8	7410.408*			
6	6	7079.434			
	7	7218.001	7217.703	−0.698	
	8	7375.687	7375.100	−0.587	
	9	7552.554	7550.724	−1.830	

[a] Term values obtained by adding ground state energies from Ref. [15] to reported wavenumbers from Ref. [19].
[b] Asterisks indicate term values not included in subsequent fitting. These are believed to be perturbed on the basis of irregularities in difference table trends or anomalously large (obs–calc) residuals.
[c] The $2v_4^0$ splittings are calculated from wavenumbers reported in Refs. [16] and [17] and the ground state energies of Ref. [15].

deviations of the fits. The latter are large, showing that the simple linear formulas do not represent the data well and that more complete multi-state models with off-diagonal interactions and inter-mode perturbation terms are really needed.

5. Discussion and conclusions

In this work, the IR spectrum of NH_3 has been recorded at high sensitivity from 6460 to 6522 cm^{-1} employing an external cavity tunable diode laser source and new multipass optics installed in a large molecular beam chamber. The study was initiated as a stringent test of the optical system, and also to supplement previous FTIR observations in this region [19] by exploring the extent of weaker absorption lines in the spectrum. Many weak features were indeed observed, giving an overall line density of over 13 lines per cm^{-1}, about three times as many as originally reported in the FTIR investigation [19]. This dense background of

Table 3
Additional proposed transition assignments in the $(\nu_1 + \nu_3)$ band of NH_3

Proposed assignment						Wavenumber [a] (cm^{-1})	Absorption strength[b]	Upper energy[c] (cm^{-1})
J'	K'	l'	J''	K''	Inv.			
2	2	1	1	1	*a*	6636.185	4.1940	6653.148[e]
2	2	−1	3	3	*s*[d]	6568.299	7.5556	6654.161
					a[d]	6568.401	7.6015	6655.059
3	3	−1	4	4	*s*[d]	6555.679	4.0950	6695.037
					a[d]	6555.991	3.7873	6696.154
4	4	−1	5	5	*s*[d]	6542.420	3.2486	6747.689
					a[d]	6542.619	3.3553	6748.706
5	5	−1	6	6	*s*[d]	6528.894	4.4665[f]	6812.468
					a[d]	6528.894	4.4665[f]	6813.304
5	2	−1	5	3	*a*	6628.970	2.7887	6894.197
			6	3	*a*	6510.219	2.3447	6894.196
5	4	1	4	3	*s*	6678.533	8.3875	6843.864
6	1	−1	5	2	*s*	6741.329	0.2229	7024.266
			6	2	*s*	6622.620	0.9326	7024.268
			7	2	*s*	6484.425	0.3344	7024.270
6	3	1	5	2	*s*	6705.963	1.2854	6988.900
			6	2	*s*	6587.255	3.7030[f]	6988.903
6	3	1	5	2	*a*	6705.335	1.7267	6988.952
			6	2	*a*	6586.675	1.6166	6988.953
7	1	−1	7	2	*s*	6623.327	0.4504	7163.172
			8	2	*s*	6465.778[g]	[0.58][g]	7163.173

[a] Wavenumbers are from Ref. [19], except for the last entry.
[b] Absorption strength from Ref. [19], in units of 10^{-4} cm^{-1}/Torr.
[c] Upper state term values obtained by adding ground state energies from Ref. [15] to the reported transition wavenumbers.
[e] Upper state energy agrees with the value of 6653.147 cm^{-1} reported in Ref. [21] as determined from the $^rQ\ 2_2 \leftarrow 2_1$ *a* transition.
[d] Inversion *a* and *s* symmetry labeling is tentative.
[f] Blended line.
[g] Wavenumber measured in present work, with observed intensity scaled for consistency with Ref. [19].

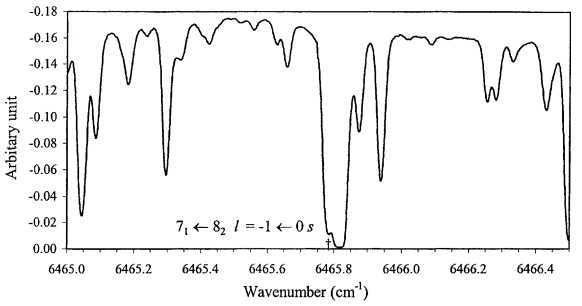

Fig. 8. Segment of the experimental spectrum showing line at 6465.778 cm^{-1} assigned as the $7_1 \leftarrow 8_2$ $l = -1 \leftarrow 0$ *s* transition of the $(\nu_1 + \nu_3)$ band of NH_3.

weak absorptions will contribute to the apparent band strength of NH_3 in this region, so would need to be considered when seeking to determine accurate band profiles and band intensities.

Originally, random frequency jitter and varying linewidths were encountered in the spectral plots produced from the computer-acquired data. These problems arose because the line wavenumbers in the study were determined with a wavemeter of nominal resolution of only ±0.01 cm^{-1}, and because the sweeps of the TDL source were nonlinear over the 1 cm^{-1} ranges of the fine-tuning PZT scans. However, by use of calibration curves relating the wavemeter readings to the diode PZT scanning voltage, we were able to linearize the spectral scans and improve the wavenumber accuracy to an estimated ±0.005 cm^{-1} by interpolation. A list of some 818 absorption lines from 6460 to 6522 cm^{-1} with peak wavenumbers, absorption

Table 4
Effective linear Hamiltonian parameters (in cm^{-1}) for the $(v_1 + v_3)$ and $2v_3^0$ states of NH_3 and comparison to the ground state[a]

Parameter (cm^{-1})	Matrix element	$(v_1 + v_3)$		$2v_3^0$		Ground state[b]	
		s	*a*	*s*	*a*	*s*	*a*
E_o	1	6608.8226	6609.7640	6795.9637	6795.4633	0.0000	0.7932
B	$J(J+1)$	9.9500	9.9444	9.5264	9.6176	9.9466	9.9416
$C - B$	K^2	−3.8309	−3.8405	−3.2639	−3.5594	−3.7190	−3.7121
$D_J \times 10^4$	$-[J(J+1)]^2$	8.3370	21.6163	−24.4334	8.1297	8.4578	8.3142
$D_{JK} \times 10^4$	$-J(J+1)K^2$	−24.5772	−59.0978	−5.4133	−83.8542	−15.6913	−15.2923
$D_K \times 10^4$	$-K^4$	5.9024	23.9308	29.1902	21.0836	9.0824	8.8063
$H_{JJJ} \times 10^7$	$[J(J+1)]^6$	–[c]	–[c]	–[c]	–[c]	2.2295	2.0471
$H_{JJK} \times 10^7$	$[J(J+1)]^4K^2$	–[c]	–[c]	–[c]	–[c]	−8.0127	−7.2506
$H_{JKK} \times 10^7$	$J(J+1)K^4$	–[c]	–[c]	–[c]	–[c]	9.7337	8.6684
$H_{KKK} \times 10^7$	K^6	–[c]	–[c]	–[c]	–[c]	−3.7996	−3.2975
$2C\zeta$	$-Kl$	0.3456	0.2245				
η_J	$J(J+1)Kl$	−0.0088	−0.0112				
η_K	K^3l	0.0002	−0.0012				
S.D.		0.4563	0.5248	0.8824	0.5402		

[a] The linear diagonal Hamiltonian model used for the term values is the sum of the products of the parameters in the first column times the matrix elements in the second column. Note that an additional parameter ρ representing splitting of the $K = 3$ energy levels [15] is not included here, as this term is expected to make a negligible contribution for the J value range in the present work.

[b] Ground state parameters were taken from Ref. [15].

[c] The sixth-order H parameters were fixed to ground state values for the $(v_1 + v_3)$ and $2v_3^0$ states in the fits.

strengths and line widths has been compiled, and is available from the authors on request.

To explore possible systematics in the energy structures of the $(v_1 + v_3)$ and $2v_3^0$ excited vibrational states in our region, upper level term value maps were generated from the results of previous FTIR and TDL studies and the trends in the *l*-doubling and *a*–*s* splittings were examined. The variations in the *l*-doubling and inversion splittings with J are much larger and more irregular for the $(v_1 + v_3)$ and $2v_3^0$ states than for the fundamental v_1 and v_3 parents. On the basis of the reported assignments and the parallel nature of the $2v_3^0$ overtone band, the inversion doubling of the $2v_3^0$ levels appears to be inverted, with a/s ordering opposite to that for the $2v_4^0$ state. Trends in the $(v_1 + v_3)$ term value wavenumbers and intensities were exploited to come up with 21 further proposed assignments for $(v_1 + v_3)$ transitions. The $(v_1 + v_3)$ and $2v_3^0$ term values were fitted to simple semi-empirical linear formulas incorporating just the diagonal terms in an effective Hamiltonian, to assess the possible extent of perturbations, off-diagonal interactions and intermode coupling. Large standard deviations in the fits and erratic variations in the term value trends indicate that higher-order coupling terms are indeed important, as found for other modes of NH_3.

Acknowledgements

This research was supported financially by the Canadian Institute for Photonic Innovations (CIPI), under the Networks of Centres of Excellence program, and by the Natural Sciences and Engineering Research Council of Canada. M.Y.T. acknowledges partial support from the Russian Fund for Basic Research and the Russian Ministry of Sciences and Technologies. The authors are grateful to J.-U. Grabow, G. Golubiatnikov and I. Leonov for advice during the early stages of the experimental design and setup, Dr. J.O. Henningsen for providing a machine readable list of the NH_3 lines from Ref. [19], and I. Koval for assistance with the data analysis. We thank Dr. D. Tokaryk for providing us with a copy of his data acquisition program written in Basic.

References

[1] C.E. Cleeton, N.H. Williams, Phys. Rev. 45 (1934) 234.
[2] C.H. Townes, A.L. Schawlow, Microwave Spectroscopy, McGraw-Hill, New York, 1955.
[3] S.K. Atreya, Atmospheres and Ionospheres of the Outer Planets and Their Satellites, Springer-Verlag, Berlin, Heidelberg, 1986.
[4] A.C. Cheung, D.M. Rank, C.H. Townes, D.D. Thornton, W.J. Welch, Phys. Rev. Lett. 21 (1968) 1701.
[5] T. Fouchet, E. Lellouch, B. Bézard, T. Encrenaz, P. Drossart, H. Feuchtgruber, T. de Graauw, Icarus 143 (2000) 223.
[6] M.E. Webber, D.S. Baer, R.K. Hanson, Appl. Opt. 40 (2001) 2031.
[7] L.S. Rothman et al., J. Quant. Spectrosc. Radiat. Transfer 60 (1998) 665.
[8] S. Urban, J. Quant. Spectrosc. Radiat. Transfer 48 (1992) 675.
[9] S. Urban, V. Spirko, D. Papousek, R.S. McDowell, N.G. Nereson, S.P. Belov, L.I. Gershstein, A.V. Maslovskij, A.F. Krupnov, J. Curtis, K.N. Rao, J. Mol. Spectrosc. 79 (1980) 455.
[10] S.P. Belov, L.I. Gershstein, A.F. Krupnov, A.V. Maslovskij, S. Urban, V. Spirko, D. Papousek, J. Mol. Spectrosc. 84 (1980) 288.
[11] S. Urban, V. Spirko, D. Papousek, J. Kauppinen, S.P. Belov, L.I. Gershstein, A.F. Krupnov, J. Mol. Spectrosc. 88 (1981) 274.
[12] S. Urban, D. Papousek, J. Kauppinen, K. Yamada, G. Winnewisser, J. Mol. Spectrosc. 101 (1983) 1.
[13] E.A. Cohen, R.L. Poynter, J. Mol. Spectrosc. 53 (1974) 131.
[14] E.A. Cohen, J. Mol. Spectrosc. 79 (1980) 496.
[15] S. Urban, R. D'Cunha, K.N. Rao, D. Papousek, Can. J. Phys. 62 (1984) 1775.
[16] G. Guelachvili, A.H. Abdullah, N. Tu, K.N. Rao, S. Urban, D. Papousek, J. Mol. Spectrosc. 133 (1989) 345.
[17] I. Kleiner, L.R. Brown, G. Tarrago, Q.-L. Kou, N. Picque, G. Guelachvili, V. Dana, J.-Y. Mandin, J. Mol. Spectrosc. 193 (1999) 46.
[18] L.R. Brown, J.S. Margolis, J. Quant. Spectrosc. Radiat. Transfer 56 (1996) 283.
[19] L. Lundsberg-Nielsen, F. Hegelund, F.M. Nicolaisen, J. Mol. Spectrosc. 162 (1993) 230.
[20] W.S. Benedict, E.K. Plyler, Can. J. Phys. 35 (1957) 1235.
[21] G. Berden, R. Peeters, G. Meijer, Chem. Phys. Lett. 307 (1999) 131.
[22] T.A. Hu, E.L. Chappell, T. Munely, S.W. Sharpe, Rev. Sci. Instrum. 64 (1993) 3380.
[23] S.L. Coy, K.K. Lehmann, Spectrochim. Acta 45A (1989) 47.